Songklanakarin J. Sci. Technol.
42 (2), 339-345, Mar. - Apr. 2020

http://www.sjst.psu.ac.th

Original Article

Effect of stress path on shearing resistance of sandstone fractures

Pakpoom Naphudsa, Thanittha Thongprapha, and Kittitep Fuenkajorn*

Geomechanics Research Unit, Institute of Engineering,
Suranaree University of Technology, Mueang, Nakhon Ratchasima, 30000 Thailand

Received: 9 August 2018; Revised: 3 October 2018; Accepted: 22 December 2018

Abstract

Triaxial and direct shear tests have been performed on rough (tension-induced) and smooth (saw-cut) fractures in Phra Wihan sandstone specimens. Two stress paths are used for the triaxial shear testing: constant confining stress and constant mean stress. It is found that under low confinement both stress paths show similar shearing resistance for the rough fractures. Under high confinement, however, the strengths under constant mean stress are notably lower than those of constant confining stress. The shear strengths of smooth fractures are independent of the stress path. This is supported by the shear strength results obtained from the direct shear testing, which suggests that under low normal stress and unconfined condition the stress path effect is insignificant. It is postulated that fracture roughness and non-linear behavior of fracture wall rock under high confinements are the main factors that cause stress path dependency of rock fractures.

Keywords: shear strength, strain energy density, Coulomb criterion, mean stress, triaxial test

1. Introduction

A principal concern of stress path appears when the triaxial compressive strength of rock obtained from laboratory testing under conventional loading path (constant confining pressure) tends to be higher than those under in-situ conditions where the mean stress near opening boundary remains constant before and after excavation (Martin, 1997). Application of the laboratory test results may therefore lead to a non-conservative analysis and design of relevant geologic structures. The effects of stress path on strength and deformability of intact rocks have long been recognized. There are two contradictory opinions; one regards that the rock strength is independent of stress path (Crouch, 1972; Swanson & Brown, 1971; Yang, Jing, & Wang, 2012). Another opinion suggests that the stress path has a significant effect on the rock strength (Artkhonghan, Sartkaew, Thongprapha, & Fuenkajorn, 2018; Melati, Wattimena, Kramadibrata, Simangunsong, & Sianturi, 2014; Mellegard & Pfeifle, 1999; Qin *et al*., 2018; Yang, Jing, Li, & Han, 2011). Hudson and Harrison (2002) conclude that the strength of rocks is dependent of stress path for inelastic material, but has no significant effect on elastic material. Several researchers have experimented and investigated various factors controlling the shear strength behavior of rock fractures. These include, for examples, effect of true triaxial stresses on sandstone fractures (Kapang, Walsri, Sriapai, & Fuenkajorn, 2013), effects of cyclic shear loading on granite, sandstone and limestone fractures (Kamonphet, Khamrat, & Fuenkajorn, 2015), effect of displacement velocity on granite, sandstone and marl fractures (Kleepmek, Khamrat, Thongprapha, & Fuenkajorn, 2016), and thermal effect on granite fractures (Khamrat, Thongprapha, & Fuenkajorn, 2018). No attempt however has been made to assess the effects of stress path on the fracture shear strength, as addressed by Naiguang, Jinsheng, Jihan, and Xiaohong (1987) and Tisa and Kavári (1984). In particular, the triaxial shear test under the constant mean stress path, which is similar to the shearing behavior of fractures around underground opening, has never been performed.

The objective of this study is to experimentally determine the shearing resistance of tension-induced fractures and smooth saw-cut surfaces under different stress paths. A true triaxial load frame is used to conduct triaxial shear test by shearing rock fractures under constant mean stress (σ_m) and under constant confining stress (σ_o). Direct shear tests are also performed to determine the fracture shear strength under

*Corresponding author
Email address: kittitep@sut.ac.th

constant normal stress (σ_n) and under constant shear stress (τ). Similarity and discrepancy of the strength results are identified based on the Coulomb criterion. Strain energy density principle is applied to calculate the energy from the fracture shear strengths and displacements, and hence allows determining the distortional strain energy densities required to shear the sandstone fractures under various stress states.

2. Sample Preparation

Rock specimens tested in this study are prepared from Phra Wihan sandstone. The sandstone is classified as fine-grained quartz with highly uniform texture and density. Related study performed by Khamrat, Archeeploha, and Fuenkajorn (2016) has determined the mineral compositions and mechanical properties of the sandstone obtained from the same source location. It comprises 72% quartz (0.2-0.8 mm), 20% feldspar (0.1-0.8 mm), 3% mica (0.1-0.3 mm), 3% rock fragments (0.5-2 mm), and 2% other (0.5-1 mm). The average density is 2.21±0.25 g/cc. The uniaxial compressive strength is 48±11 MPa, cohesion is 10 MPa, and internal friction angle is 46°. Based on the classification by International Society for Rock Mechanics (Brown, 1981) the sandstone is classified as medium strong rock.

The sandstone specimens prepared for the triaxial shear test have nominal dimensions of 50×50×87 mm^3. A line load is applied to obtain a tension-induced fracture diagonally across the block specimen. The smooth fractures are artificially made by using a universal masonry saw (Husqvarna TS400F). They are also cut along the diagonal line of the specimen. The prepared fractures have nominal areas of 50× 100 mm^2. The normal to the fracture plane makes an angle (β) of 60° with the main axis of the specimen.

The specimens for direct shear testing are prepared to have nominal dimensions of 100×100×160 mm^3. The tension-induced and saw-cut fractures are made at the mid-section of the specimens. The fracture area is 100×100 mm^2. All fractures are clean and well mated.

The asperity amplitudes for the rough (tension-induced) fractures are measured from the laser-scanned profiles along the shear direction. The fracture profile readings are made to the nearest 0.001 mm. The maximum amplitudes are used to determine the joint roughness coefficients (JRC) of each fracture by using Barton's chart (Barton, 1982). The JRC values averaged from all rough fractures are 7.6±0.5.

3. Test Apparatus and Methods

The triaxial shear test is performed by using a true triaxial load frame (Komenthammasopon, 2014), as shown in Figure 1. The device comprises four main components: three mutually perpendicular load frames, six 100-ton hydraulic cylinders, measurement system and three hydraulic pumps. The measurement system includes pressure transducers, displacement transducers, switching box, and data logger. One of the lateral (horizontal) stresses is parallel to the strike of the fracture plane and is designated as σ_p. The other is normal to the fracture strike and is designated as σ_o.

Testing for the constant σ_o path, which is similar to the conventional triaxial shear method, is conducted under constant lateral stresses (σ_o=σ_p) from 1, 3, 7, 12 to 18 MPa. At first, the axial (σ_1) and lateral stresses are simultaneously increased to the predefined magnitude of σ_o where the shear stress on the fracture plane is zero. The axial stress is then increased at the rate of 0.1 MPa/s while the lateral stresses are maintained constant until peak shear strength is reached (Table 1a). The test is terminated when an axial displacement of 5 mm is obtained.

The triaxial shear test for constant σ_m path uses the mean stress [(σ_1+ σ_o+ σ_p) / 3], which ranges from 20, 25, 30, 35, 40, 45, 50 to 55 MPa. The σ_1 and lateral stresses (σ_o and σ_p) are first simultaneously increased to the predefined magnitude of σ_m where the τ on the fracture plane is zero. The σ_1 is then increased at the rate of 0.1 MPa/s while σ_o is decreased under the same rate. The σ_p is maintained constant during the test (Table 1b). The test is terminated after the peak shear strength is reached. The specimen deformations are monitored along the three principal loading directions. They are used to calculate the principal strains during loading.

The τ and its corresponding σ_n for the triaxial shear test can be determined as follows (Jaeger, Cook, & Zimmerman, 2007):

$$\tau = \frac{1}{2}(\sigma_1 - \sigma_o)\cdot\sin2\beta \quad (1)$$

$$\sigma_n = \frac{1}{2}(\sigma_1 + \sigma_o) + \frac{1}{2}(\sigma_1 - \sigma_o)\cdot\cos2\beta \quad (2)$$

where β is the angle between σ_1 and σ_n directions. For all specimens, the angle β equals to 60°. The shear and normal displacements (d_s and d_n) can also be determined from the axial and lateral displacements (d_1 and d_o) as follows (Kleepmek *et al*., 2016):

$$d_s = d_1\cdot\sin\beta \quad (3)$$

$$d_n = (d_{o,m}-d_{o,c})\cdot\sin\beta \quad (4)$$

$$d_{o,c} = d_1\cdot\tan(90-\beta) \quad (5)$$

where $d_{o,m}$ is the total lateral displacement measured during the test, and $d_{o,c}$ is the calculated lateral displacement induced

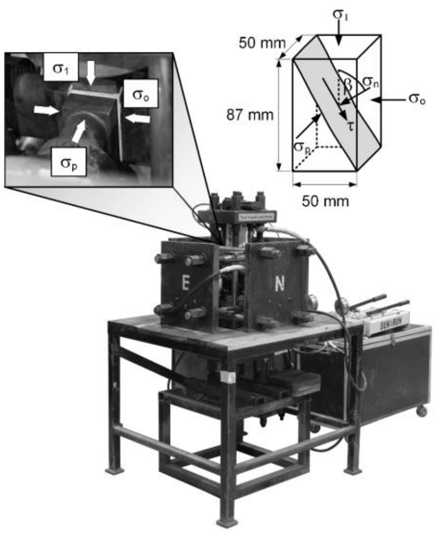

Figure 1. True triaxial load frame used to apply three principal stresses, to triaxial shear test specimen.

Table 1. Stress paths of shear tests.

Test method	Stress path	
	(a) Constant σ_o	(b) Constant σ_m
Triaxial shear test	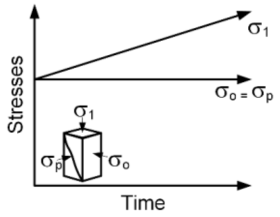	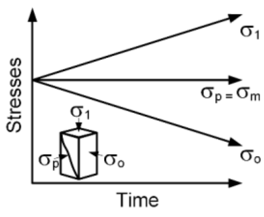
	σ_o = 1–18 MPa	σ_m = 20–55 MPa
	(c) Constant σ_n	(d) Constant τ
Direct shear test	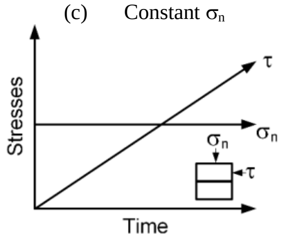	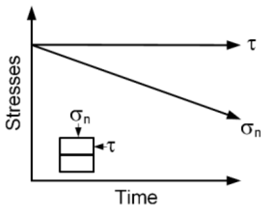
	σ_n = 1–4 MPa	τ = 1–4 MPa

by the axial displacement on the inclined fracture plane. The induced fracture dilation along σ_o axis can be determined by subtracting the calculated dilation caused by the inclined fracture plane from the measured dilation ($d_{o,m}$), as shown in Equation (5).

The direct shear tests are performed by using the direct shear device (SBEL DR44). Two shear stress paths are used: constant σ_n and constant τ. The test method for constant σ_n path follows the ASTM (D5607-16) standard practice. The applied constant normal stresses σ_n are 1, 2, 3, and 4 MPa. The τ is increased at the rate of 0.1 MPa/s until a total shear displacement of 5 mm is reached (Table 1c). For testing under constant τ path the normal and shear stresses are simultaneously increased to the predefined magnitude, where before shearing $\sigma_n = \tau$, which ranges between 1, 2, 3, and 4 MPa. The shear stress is maintained constant while σ_n is conti-nuously reduced at the rate of 0.1 MPa/s. The constant τ path is terminated when dropping of the shear stress is detected (Table 1d). The normal (dilation) and shear displacements are monitored using high precision displacement gages.

4. Test Results

Figure 2 shows the shear stresses as a function of shear displacement of rough fractures for both stress paths. They are calculated from the measured axial and lateral stresses by using Equations (1) and (3). The shear stresses increase with increase of σ_o and σ_m. For the constant σ_m testing

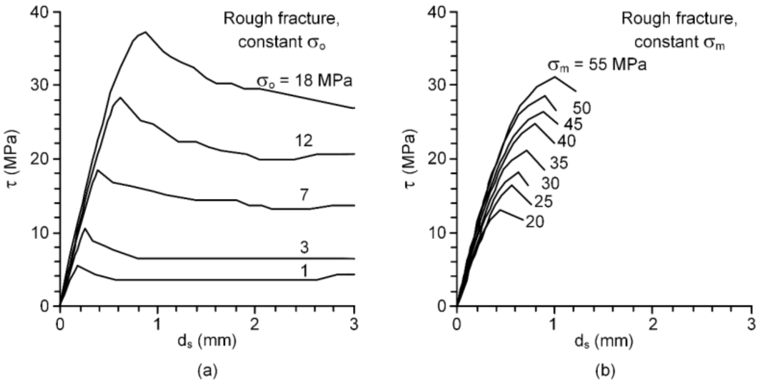

Figure 2. Shear stresses (τ) as a function of shear displacement (d_s) under constant confining stress σ_o (a) and constant mean stress σ_m (b).

the residual shear stresses cannot be obtained as the σ_m values cannot be maintained constant after the peak shear stress has been reached. Note also that the range of σ_m values used for constant σ_m testing is relatively high compared to the σ_o values used in the constant σ_o testing. This is primarily because when σ_m is lower than 20 MPa the decreasing σ_o reaches zero before the peak shear stress is reached.

The peak shear stresses (τ_p) are plotted as a function of their corresponding normal stress (σ_n) in Figure 3. The normal stresses are calculated from Equation (2). The Coulomb criterion is applied to describe the fracture shear strengths obtained from both stress paths. The cohesion and friction angle for each test conditions are given in the figure. The criterion fits well to all strength results, as suggested by their good correlation coefficients (R^2 > 0.9). The shear strengths for smooth fractures obtained from both stress paths are virtually identical, suggesting that stress path have insignificant impact on their shearing behavior. For rough fractures, the shear strengths obtained from constant σ_o path tend to be greater than those from constant σ_m path, particularly under high confinements (high σ_o and σ_m values). Under low confinements both stress paths yield similar shear strengths. The diagram in Figure 3 shows the upper bound of the shear strengths (indicated by dash line) for the triaxial shear test. It is defined by angle β which is maintained constant at 60° for all specimens. This angle represents the angle between the maximum principal stress and the normal of the fracture plane, where the relationship between σ_n and σ_1 is shown in Equation (2). The lower bound strength is defined by the basic friction angle (ϕ_b) obtained from the smooth fracture testing.

To confirm the conclusions drawn above series of direct shear testing have been performed on the rough fracture. The test results are obtained for two stress paths: constant σ_n and constant τ. Figure 4 shows the shear stresses (τ) as functions of shear displacement (d_s). Higher normal stresses (σ_n) are applied, higher shear stresses are obtained. The strength results from both stress paths are very similar, as shown in Figure 5. This suggests that under low normal stresses and unconfined condition the effect of stress path may not exist, which agrees with the shear strength results obtained from the triaxial shear tests under low confinement with different stress paths.

The friction angles of rough fractures obtained from triaxial shear tests are lower than that from the direct shear test. This is due to the fact that the lateral stress parallel to fracture plane, σ_p, of the triaxial test has caused localized stress concentration at the fracture asperities, and hence weakens the fracture wall rock. This behavior has also been observed by Kapang *et al*. (2013).

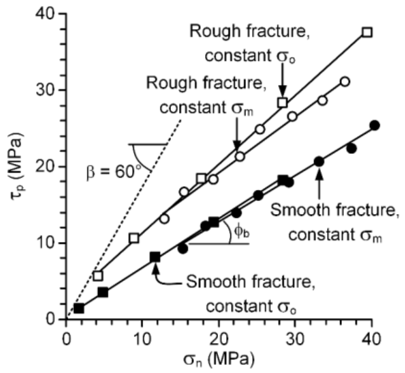

Rough fractures

Stress path	$\tau_p = \sigma_n \tan\phi_p + c$ c (MPa)	ϕ_p (°)	R^2
Constant σ_o	2.25	42.0	0.998
Constant σ_m	4.58	36.1	0.983

Smooth fractures

Stress path	$\tau_p = \sigma_n \tan\phi_b$ ϕ_b (°)	R^2
Constant σ_o	32.4	0.999
Constant σ_m	31.1	0.989

Figure 3. Peak shear stress (τ_p) as a function of normal stress (σ_n) for triaxial shear tests.

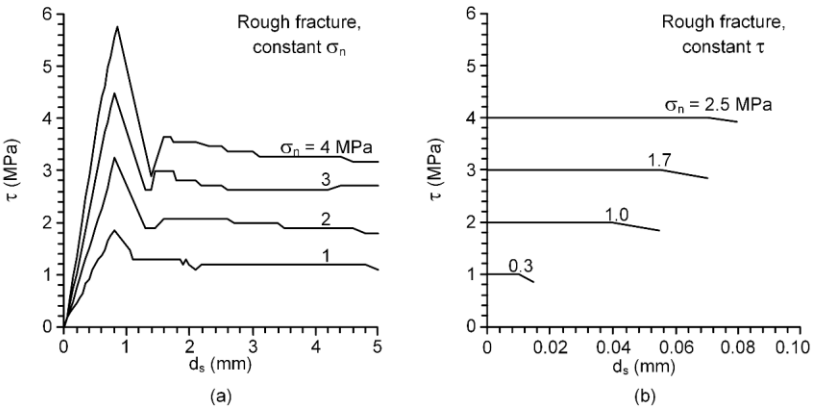

Figure 4. Shear stresses (τ) as a function of shear displacement (d_s) for direct shear tests under (a) constant normal stress (σ_n) and (b) constant shear stress (τ).

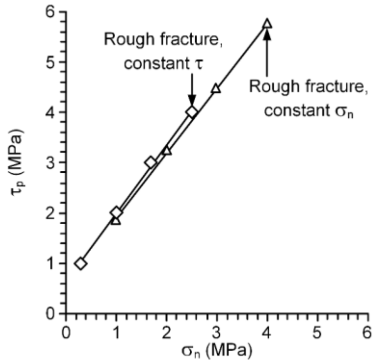

Rough fractures

Stress path	$\tau_p = \sigma_n \tan\phi_p + c$		R^2
	c (MPa)	ϕ_p (°)	
Constant σ_n	0.64	52.0	0.999
Constant τ	0.62	53.8	0.998

Figure 5. Peak shear stress (τ_p) as a function of normal stress (σ_n) for direct shear test.

5. Strain Energy Criterion

The strain energy density principle is proposed here to describe fracture shear strengths under both stress paths. It considers both stress and displacement at failure, and hence allows a more rigorous assessment of the sheared fracture behavior. The distortional strain energy (W_d) required to displace the fractures can be defined as a function of mean strain energy (W_m) as follows (Khamrat *et al*., 2018):

$$W_d = \delta \cdot W_m \tag{6}$$

where δ is an empirical constant. The distortional and mean strain energy can be calculated from the test results as follows (Jaeger *et al*., 2007):

$$W_d = 3/2\ \tau_{oct} \cdot \gamma_{oct} \tag{7}$$
$$W_m = 3/2\ \sigma_m \cdot \varepsilon_m \tag{8}$$

where τ_{oct} and γ_{oct} are octahedral shear stress and strain, and σ_m and ε_m are mean stress and mean strain. Note that the strain that is parallel to the fracture strike is equal to zero ($\varepsilon_p = 0$) because the test configurations (loading platens) do not allow lateral displacement in this direction. As a result, the shear and mean stress and strain at the peak point can be determined as:

$$\tau_{oct} = (1/3)\ [(\sigma_{1,p} - \sigma_{p,p})^2 + (\sigma_{p,p} - \sigma_{o,p})^2 + (\sigma_{o,p} - \sigma_{1,p})^2]^{1/2} \tag{9}$$
$$\gamma_{oct} = (1/3)\ [\varepsilon_{1,p}^2 + \varepsilon_{o,p}^2 + (\varepsilon_{1,p} - \varepsilon_{o,p})^2]^{1/2} \tag{10}$$
$$\sigma_m = (\sigma_{1,p} + \sigma_{p,p} + \sigma_{o,p}) / 3 \tag{11}$$
$$\varepsilon_m = (\varepsilon_{1,p} + \varepsilon_{o,p}) / 3 \tag{12}$$

where $\sigma_{1,p}$ is maximum axial stress at peak shear stress, $\sigma_{p,p}$ is lateral stresses paralleled to strike of fracture plane at peak shear stress, $\sigma_{o,p}$ is stresses normal to fracture strike at peak shear stress, $\varepsilon_{1,p}$ is maximum axial strain at peak shear stress, and $\sigma_{o,p}$ is strain normal to fracture strike at peak shear stress. Assuming that the intact portion of the specimen is rigid, the axial and lateral strains can be measured from the fracture displacements (Khamrat *et al*., 2018):

$$\varepsilon_{1,p} = d_{1,p} / L \tag{13}$$
$$\varepsilon_{o,p} = d_{o,p} / W \tag{14}$$

where $d_{1,p}$ and $d_{o,p}$ are the axial and lateral displacements normal to the fracture strike, L is the specimen length (87 mm), and W is the specimen width (50 mm). Tables 2 and 3 give the distortional and mean strain energy calculated for the rough and smooth fractures for the two stress paths.

Regression analysis of the test results against Equation (6) indicates that δ equals to 3.84 for the rough fractures and 2.11 for the smooth fractures (Figure 6). The strain energy equation proposed by Khamrat *et al*. (2018) (Eq. (6)) fits well to the test data with the correlation coefficient (R^2) greater than 0.9. It implicitly incorporates the effects of stress path on the fractures, as their calculated energy densities are coincided and can be represented by a failure envelope. The mean strain energy can be related to the depth of the fractures. The distortional strain energy represents the deviatoric stresses that cause the shear displacement. Khamrat *et al*. (2018) state that the ratio of W_d to W_m is governed by the roughness and strength of the fracture asperities. Rougher fractures with

Table 2. Distortional and mean strain energy densities of rough fractures under different stress paths.

Stress path	$\sigma_{p,p}$ (MPa)	$\sigma_{o,p}$ (MPa)	$\sigma_{1,p}$ (MPa)	$d_{1,p}$ (mm)	$d_{o,p}$ (mm)	$\varepsilon_{1,p}$ ($\times 10^{-3}$)	$\varepsilon_{o,p}$ ($\times 10^{-3}$)	W_d (MPa)	W_m (MPa)
Constant σ_o	1.00	1.00	13.87	0.155	-0.044	1.782	-0.883	0.010	0.002
	3.00	3.00	27.52	0.225	-0.073	2.586	-1.467	0.027	0.006
	7.00	7.00	49.66	0.340	-0.113	3.908	-2.250	0.072	0.018
	12.00	12.00	77.32	0.530	-0.163	6.092	-3.250	0.168	0.048
	18.00	18.00	104.56	0.755	-0.255	8.678	-5.100	0.324	0.084
Constant σ_m	20.00	3.74	35.48	0.385	-0.140	4.425	-2.800	0.055	0.016
	25.00	4.43	44.31	0.485	-0.190	5.575	-3.800	0.090	0.022
	30.00	7.46	50.72	0.54	-0.220	6.207	-4.400	0.111	0.027
	35.00	9.07	59.49	0.615	-0.240	7.069	-4.800	0.145	0.040
	40.00	9.60	68.40	0.685	-0.280	7.874	-5.600	0.193	0.045
	45.00	11.84	75.60	0.760	-0.310	8.736	-6.200	0.228	0.057
	50.00	15.79	83.29	0.780	-0.320	8.966	-6.400	0.254	0.064
	55.00	17.23	90.66	0.865	-0.350	9.943	-7.000	0.304	0.081

Table 3. Distortional and mean strain energy densities of smooth fractures under different stress paths.

Stress path	$\sigma_{p,p}$ (MPa)	$\sigma_{o,p}$ (MPa)	$\sigma_{1,p}$ (MPa)	$d_{1,p}$ (mm)	$d_{o,p}$ (mm)	$\varepsilon_{1,p}$ ($\times10^{-3}$)	$\varepsilon_{o,p}$ ($\times10^{-3}$)	W_d (MPa)	W_m (MPa)
Constant σ_o	1.00	1.00	4.13	0.640	-0.183	7.356	-3.667	0.010	0.004
	3.00	3.00	11.01	0.660	-0.192	7.586	-3.833	0.025	0.011
	7.00	7.00	25.80	0.690	-0.200	7.931	-4.000	0.062	0.026
	12.00	12.00	41.28	0.710	-0.208	8.161	-4.167	0.100	0.043
	18.00	18.00	60.20	0.750	-0.217	8.621	-4.333	0.152	0.069
Constant σ_m	20.00	9.96	30.96	0.600	-0.210	6.897	-4.200	0.058	0.027
	25.00	11.34	39.56	0.640	-0.220	7.356	-4.400	0.083	0.037
	30.00	14.45	46.44	0.670	-0.230	7.644	-4.600	0.098	0.046
	35.00	15.84	53.32	0.690	-0.240	7.931	-4.800	0.119	0.054
	40.00	18.95	60.20	0.710	-0.250	8.161	-5.000	0.136	0.063
	45.00	21.30	68.80	0.740	-0.260	8.506	-5.200	0.163	0.074
	50.00	24.41	75.68	0.760	-0.265	8.736	-5.300	0.180	0.086
	55.00	25.79	84.28	0.780	-0.270	8.966	-5.400	0.210	0.098

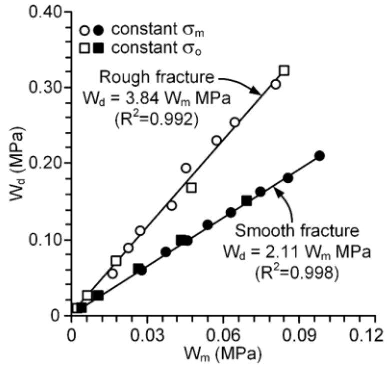

Figure 6. Distortion strain energy density (W_d) as a function of mean strain energy density (W_m) for rough and smooth fractures.

strong wall rock would give higher δ value than that of smoother fractures with weaker rock wall. The W_d-W_m curve (Figure 6) of the smooth fractures would represent the lower bound of the energy required to shear the rock fractures.

6. Discussion and Conclusions

The results clearly indicate that under high confinements the shear strengths of rough fractures under constant σ_m path is lower than those of the constant σ_o path. For intact rock, Artkhonghan *et al*. (2018), Mellegard and Pfeifle (1999) and Weng and Ling (2013) propose an explanation for the constant σ_m path that when σ_1 is increased as the σ_2 and/or σ_3 are decreased, the dilation occurs along the σ_2 and/or σ_3 directions. This makes the rocks fail more easily under constant σ_m path. This postulation can help explaining the difference of the fracture shear strengths obtained under different stress paths here.

Both stress paths yield similar shearing resistance of the rough fractures for the direct shear testing. This is because the fractures are under low confinement. The smooth fracture is independent of stress path, which agrees with the result obtained by Tisa and Kovári (1984) who perform the different stress paths on smooth fractures in granite. The shear strengths of the rough and smooth fractures can be well described by the Coulomb criterion.

The distortional and mean strain energy densities are calculated from the test results. Their linear relation has implicitly incorporated the effects of the stress paths (Figure 6). The ratio of the W_d-W_m (δ) depends on the fracture roughness and strength of the asperities. All deformations are from the shear and dilation within the fracture with the assumption that the rock adjacent to a fracture is rigid. Recognizing the effects of stress path on the fracture shear strength under high confining pressures would be useful to obtain a more conservative analysis and design of underground openings in rock mass.

Acknowledgements

This research is funded by Suranaree University of Technology and by the Higher Education Promotion and National Research University of Thailand. Permission to publish this paper is gratefully acknowledged.

References

Artkhonghan, K., Sartkaew, S., Thongprapha, T., & Fuenkajorn, K. (2018). Effects of stress path on shear strength of a rock salt. *International Journal of Rock Mechanics and Mining Sciences, 104*, 78-83.

ASTM International. (2016). *Standard test method for performing laboratory direct shear strength tests of rock specimens under constant normal force. ASTM D5607-16*. West Conshohocken, PA: Author.

Barton, N. (1982). Shear strength investigations for surface mining. In C. O. Brawner (Ed.), *3rd International Conference on Stability in Surface Mining* (pp. 171-192). New York, NY: Society of Mining Engineers of AIME.

Brown, E. T. (1981). *Rock characterization testing and monitoring: ISRM suggested methods.* New York, NY: Pergamon Press.

Crouch, S. (1972). A note on post-failure stress-strain path dependence in norite. *International Journal of Rock Mechanics and Mining Sciences, 9*(2), 197-204.

Hudson, J. A., & Harrison, J. P. (2002). Principal of the stress path and its visualization for rock mechanics and rock engineering. *Proceedings of the 2nd*

International Conference on New Development in Rock Mechanics and Rock Engineering. Liaoning, China.

Jaeger, J. C., Cook, N. G. W., & Zimmerman, R. W. (2007). *Fundamentals of rock mechanics* (4th ed). Massachusetts, MA: Blackwell Publishing.

Kamonphet, T., Khamrat, S., & Fuenkajorn, K. (2015). Effects of cyclic shear loads on strength, stiffness and dilation of rock fractures. *Songklanakarin Journal of Science and Technology, 37*(6), 683-689.

Kapang, P., Walsri, C., Sriapai, T., & Fuenkajorn, K. (2013). Shear strengths of sandstone fractures under true triaxial stresses. *Journal of Structural Geology, 48*, 57-71.

Khamrat, S., Archeeploha, S., & Fuenkajorn, K. (2016). Pore pressure effects on strength and elasticity of ornamental stones. *ScienceAsia, 42*(2), 121-135.

Khamrat, S., Thongprapha, T., & Fuenkajorn, K. (2018). Thermal effects on shearing resistance of fractures in Tak granite. *Journal of Structural Geology, 111*, 64-74.

Kleepmek, M., Khamrat, S., Thongprapha, T., & Fuenkajorn, K. (2016). Displacement velocity effects on rock fracture shear strengths. *Journal of Structural Geology, 90*, 48-60.

Komenthammasopon, S. (2014). *Effects of stress path on rock strength under true triaxial condition* (Master's thesis, Suranaree University of Technology, Nakhon Ratchasima, Thailand).

Martin, C. D. (1997). Seventeenth Canadian Geotechnical Colloquium: The effect of cohesion loss and stress path on brittle rock strength. *Canadian Geotechnical Journal, 34*(5), 698-725.

Melati, S., Wattimena, R. K., Kramadibrata, S., Simangunsong, G. M., & Sianturi, R. G. (2014). Stress paths effects on multistage triaxial test. *Proceedings of the ISRM International Symposium 8th Asian Rock Mechanics Symposium*. Sapporo, Japan.

Mellegard, K. D., & Pfeifle, T. W. (1999). Laboratory evaluation of mechanical properties of rock using an automated triaxial compression test with a constant mean stress criterion. In W. A. Mart & C. E. Fair-hurst (Eds.), *Nondestructive and Automated Testing for Soil and Rock Properties* (pp. 247-257). West Conshohocken, PA: ASTM International.

Naiguang, G., Jinsheng, H., Jihan, L., & Xiaohong, L. (1987). Stress path and frictional sliding of rock. *Acta Seismologica Sinica, 9*(2), 201-207.

Qin, T., Sun, H., Liu, H., Zhang, J., Li, T., Liu, G., & Liu, Z. (2018). Experimental study on mechanical and acoustic emission characteristics of rock samples under different stress paths. *Shock and Vibration, 2018*, Article ID 4813724. doi:10.1155/2018/48137 24

Swanson, S., & Brown, W. (1971). An observation of loading path independence of fracture in rock. *International Journal of Rock Mechanics and Mining Sciences, 8*(3), 277-281.

Tisa, A., & Kovári, K. (1984). Continuous failure state direct shear tests. *Rock Mechanics and Rock Engineering, 17*(2), 83-95.

Weng, M. C., & Ling, H. I. (2013). Modeling the behavior of sandstone based on generalized plasticity concept. *International Journal for Numerical and Analytical Methods in Geomechanics, 37*(14), 2154-2169.

Yang, S. Q., Jing, H. W., & Wang, S. Y. (2012). Experimental investigation on the strength, deformability, failure behavior and acoustic emission locations of red sandstone under triaxial compression. *Rock Mechanics and Rock Engineering, 45*(4), 583-606.

Yang, S. Q., Jing, H. W., Li, Y. S., & Han, L. J. (2011). Experimental investigation on mechanical behavior of coarse marble under six different loading paths. *Experimental Mechanics, 51*(3), 315-334.